

Design and comparison of tails for bird-scale flapping-wing robots*

M.M. Guzmán, C. Ruiz Páez, F. J. Maldonado, R. Zufferey, J. Tormo-Barbero, J.Á Acosta*, A. Ollero

*Preprint submitted to the International Conference on Intelligent Robots and Systems (IROS 21)¹

Abstract—Flapping-wing robots (so-called ornithopters) are a promising type of platform to perform efficient winged flight and interaction with the environment. However, the control of such vehicles is challenging due to their under-actuated morphology to meet lightweight requirements. Consequently, the flight control of flapping-wing robots is predominantly handled by the tail. Most ornithopters feature a tail with two degrees of freedom but the configuration choice is often arbitrary and without in-depth study. In this paper, we propose a thorough analysis of the design and in-flight performance for the three tails. Their design and manufacturing methods are presented, with an emphasis on low weight, which is critical in ornithopters. The aerodynamics of the tails is analyzed through CFD simulations and their performance compared experimentally. The advantages and performance metrics of each configuration are discussed based on flight data. Two types of 3D flight tests were carried out: aggressive heading maneuvers and level turns. The results show that an inverted V-tail outperforms the others regarding maneuverability and stability. From the three configurations, only the inverted V-Tail can perform an aggressive stable banked level turn with a radius of 3.7 m at a turning rate of 1.6 rad/s. This research work describes the impact of the tail configuration choice on the performance of bird-scale flapping-wing robots.

I. INTRODUCTION

Flapping-wing robots show promise for affordable, safe and quiet operation in natural and industrial environments. The absence of combustion engines and propellers opens a broad range of applications in proximity to humans, wildlife and structures. More specifically, physical interaction maneuvers, such as perching and landing are of strong interest. For those tasks, reliable flight control and high maneuverability is key.

Winged aircrafts achieve attitude control through control surfaces as follow [1]. The roll is controlled by the actuated surfaces at trailing edge of each wing, or *aileron*s. The non-symmetric actuation of the ailerons applies a roll torque on the aircraft. The projection of the lift force, dominant in winged aircraft creates a lateral force which results in turning. The pitch control is handled by the horizontal tail plane, or *elevator*. The yaw angle is controlled by the vertical tail surface or *rudder*. Alternatively, the rudder and elevator can be blended into two angled tail surfaces. The symmetric and asymmetric actuation of these tail flaps respectively governs the pitch and yaw. Such a configuration is commonly referred

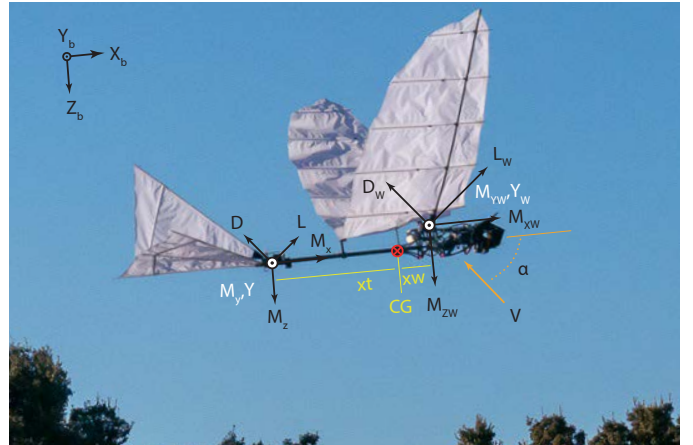


Figure 1. Side view of the flying E-Flap robot during a downstroke with the forces and moments at play on the wings and the tail.

as *V-Tail*. It can be either angled upwards or downwards (inverted).

In flapping-wing robots, the weight constraints are stricter. Actuating a single tail plane with two actuators is another existing solution that reduces the overall tail weight. Recently, researchers have demonstrated that geometric morphing of the wings can lead to an increase in maneuverability of fixed-wing robots [2]. While this is a promising technology, morphing wings in flapping robots is a challenging task due to the added weight and acceleration constraints.

Most flapping-wing robots do not have actuation in the wing. Indeed, the weight of extra control surfaces and actuation would increase the inertia of the wing, quickly degrading the vehicle efficiency. The absence of flight surfaces delegates the flight control of the robot to the tail. Therefore, careful design, manufacturing and actuation of the tail is important.

We differentiate between two control directions: the *longitudinal* and the *lateral* control. In flapping-wing vehicles, the longitudinal control is handled similarly to any winged aircraft, i.e. through the deflection of the horizontal tail surfaces. However, there is one key difference: the flapping-induced pitch oscillations which perturbs both the air flow and the servo actuation. Laterally, the lack of ailerons significantly increase the control difficulty. In this work we look for ways to improve the lateral maneuverability of a large flapping wing robot by exploring different tail configurations.

The tails of flapping-wing robots, also referred to as ornithopters, are described in the literature, as part of broader

*Corresponding author: J.Á Acosta (jaar@us.es).

¹The authors acknowledge support from the European Project GRIFFIN ERC Advanced Grant 2017, Action 788247.

¹All the authors are with the GRVC, University of Seville, Spain.

design publications. However, to the best of the author's knowledge, no published research has attempted to compare different tail configurations. Most flapping-wing projects are limited to a description or the study of a single tail configuration [3], [4], [5]. Robotics flapping-wing birds in the literature rely on one of the three tail configurations listed here below.

In this paper, we present a comparative analysis of between these three tails for flapping-wing robots:

- **D-Tail:** a double-rotating single Delta plane.
- **C-Tail:** a Conventional tail (1 rudder, 1 elevator)ⁱ.
- **V-Tail:** an inverted V tail (2 ruddervators).

Complete sizing and manufacture as well as aerodynamics characterization through CFD are reported. Moreover, the in-flight performance of three tails is experimentally compared on the *E-Flap* vehicle [6]. Longitudinal and lateral-directional tests have revealed the strengths and weaknesses between tails, and showed a better overall performance on the V-Tail.

The paper is organized as follow. First, we present an overview of the process of designing and sizing a tail for large flapping-wing robots. Three tail configurations are then discussed in terms of manufacturing and control. CFD results and experimental flight results compare the maneuverability of the different tails.

II. ORNITHOPTER TAIL SIZING

The tail of a flapping-wing robot needs to be sized, by longitudinal trim, to provide adequate control both in the longitudinal and lateral direction.

The longitudinal trim of the ornithopter is calculated as follow. The moments applied on the robot are displayed in Fig. 1. Balancing the moments around the y axis, assuming the drag force projection onto the vertical axis is negligible, gives $M_{Y_w} + L_w \cos \alpha x_w - L_t \cos \alpha x_t = 0$. The wing's and tail's lift are defined as $L_w = 1/2\rho V^2 S c_{L_w}$ and $L_t = 1/2\rho V^2 S_t c_{L_t}$, where α is the angle of attack, M_{Y_w} is the wing aerodynamic pitching moment, S is the wing surface, S_t the tail's surface, c the mean wing's chord, V for the forward speed, x_w the distance between the wing aerodynamic center and the ornithopter's center of gravity CG and x_t the distance between the CG and the tail. Non-dimensionalizing by $1/2\rho V^2 S c$ and assuming M_{Y_w} negligible since it is flat and without curvature, the following system of equations is obtained

$$c_{L_w} \frac{x_w}{c} - c_{L_t} \frac{x_t S_t}{c S} = 0, \quad c_{L_w} + c_{L_t} \frac{S_t}{S} = \frac{mg}{\frac{1}{2}\rho V^2 S} \quad (1)$$

where m is for the robot mass, ρ the air density and g the gravity. The aerodynamic wing and tail coefficients are approximated with $c_L = 2\pi\alpha \frac{AR}{AR+2}$ and $c_{L_t} = \frac{\pi}{2}\alpha AR_t$, where $AR = \frac{b^2}{S}$ and $AR_t = \frac{b_t^2}{S_t}$ are the wing and tail's aspect ratio, and b and b_t the wing and tail's span. Those coefficients were obtained by a priori modeling the aerodynamic forces following the linearized potential theory for a flat plate wing and delta tail, in gliding [7]. Substituting those coefficients in (1) yields

$$\mu = 2\pi \frac{AR}{AR+2} \alpha_{trim} + \frac{\pi}{2} \alpha_{trim} \frac{b_t^2}{S}, \quad (2)$$

ⁱAlso sometimes referred to as inverted T tail

$$4 \frac{AR}{AR+2}, \frac{x_w}{c} - \frac{b_t^2}{S} \frac{x_t}{c} = 0 \quad (3)$$

where $\mu = \frac{mg}{\frac{1}{2}\rho V^2 S}$ is the mass dimensionless parameter. Choosing 4 m/s as the design velocity and $\alpha_{trim} = 15^\circ$ as the trim angle of attack. With additional wing parameters known (the wing position $x_w = 0.13\text{m}$ has been estimated assuming a tail weight of 70 grams), a first approximation of the tail's span and tail's position can be calculated by Eq. (2) and (3), where $b_t \approx 0.5 \text{ m}$ and $x_t \approx 0.5$. Therefore, a first estimation of the geometry and position of the tail is obtained. Assuming an equilateral tail shape, the tail surface yields to $S_t \approx 0.11\text{m}^2$.

III. TAIL CONFIGURATIONS

The tail of a large flapping-wing robots can take various shapes and configurations. This section details three selected designs. The three configuration permits full tether-less flight, as verified both in simulation and experimentally.

Table I
TAILS DESIGN COMPARISON

	D-Tail	C-Tail	V-Tail
Total surface	0.11 m ²	0.11m ²	0.12 m ²
Moving surface	0.11 m ²	0.11 m ²	0.074 m ²
Fixed Surface	-	-	0.044 m ²
Chord	0.4 m	0.4 m	0.4 m
Span	0.56 m	0.56 m	0.36 m
Distance tail-CG	0.47 m	0.45 m	0.355 m
Weight	75 g	87 g	108 g
Actuation	SH-0255MG	SH-0255MG	KST 08 Plus

A. D-Tail

The D-Tail features a single actuated delta tail plane as shown in Fig. 2. This tail configuration does not possess a traditional elevator-rudder but instead relies on a serially linked double servo-actuator.

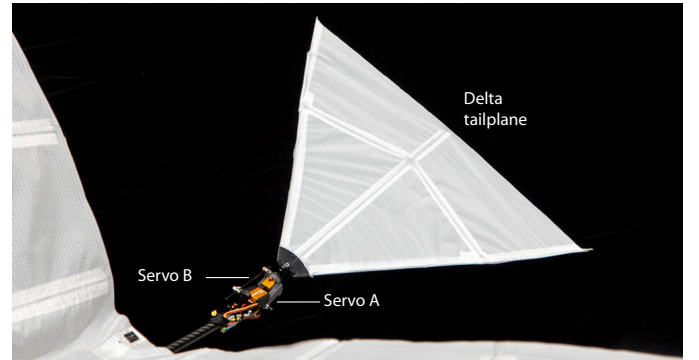


Figure 2. The D-Tail is shown with its delta tailplane actuated by 2 serially linked servos.

Several ornithopter designers have chosen this configuration [8]. For example, the Roboraven tail's size was experimentally iterated in [9] to achieve optimal solar cell disposition. Researchers qualitatively favor this configuration for its potentially lower specific weight [10].

The designed D-tail weights 75g for a 0.11 m² surface (including actuation). It is composed of three 2mm carbon fiber (CF) rods held in a 3D-printed part to give the tail its triangular form. The nylon ripstop fabric, a 48 g/m² highly

tear resistant fabric, covers the structure and is bonded to the CF rods with ripstop tape. Two orthogonal CF rods prevent the tension of the fabric from deforming the triangular shape.

The tail has 2 DoF given by two servos actuated at the root. The servo-actuators are placed in series, i.e. the base of the second servo (B) is affixed to the output of the first servo (A), as shown in Fig. 2. The A servo, directly attached to the fuselage, controls the tail pitch whereas the B servo controls the tail roll. For the first DoF, the pitch, a reduction lever transmission of 2:1 is employed to improve the resolution and reduce the torque requirements. The transmission from the roll servo to the tail is direct.

The tail pitch is used to control the longitudinal dynamics via the pitching moment of the aircraft. The tail roll is used to control the lateral-directional dynamics of the aircraft by creating a moment in yaw.

B. C-Tail

The conventional tail or C-Tail's design for our comparison consists of a 0.1 m^2 horizontal surface that entirely serves as elevator, providing longitudinal stability and a 0.05 m^2 vertical surface, i.e. the rudder, which provides directional stability.

Overall, a C-Tail provides high level of maneuverability and therefore also permits a large range of flight speeds. Low speeds are possible due to the extremely high angles of attack the ornithopter can reach with this tail, as shown in [6]. There are few ornithopters with a C-Tail. For example, the Joon Hyuk Park's ornithopter [11] features a C-Tail albeit with a fixed elevator.

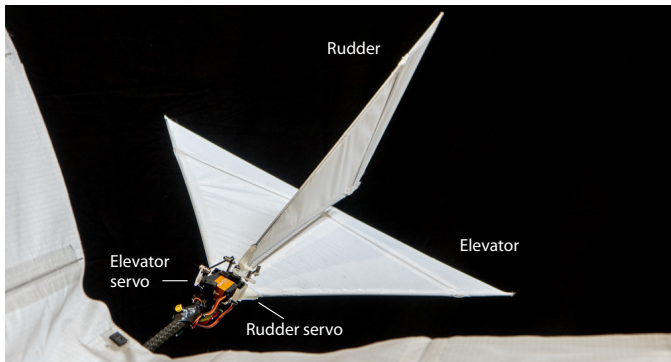


Figure 3. Photo of the C-Tail geometry based on a standard elevator-rudder configuration.

In our tail design, both horizontal and vertical surfaces are manufactured with 2mm CF rods, 3D-printed roots and nylon ripstop fabric. The horizontal surface shape is identical to the D-Tail, whilst the vertical surface is just half of the previous one. The assembly method is similar. The 2 DoF of the tail, elevator and rudder deflections, are actuated with two servos held in the fuselage with PLA connectors, as shown in Fig. 3. Similarly to the Delta tail, a lever transmission has been designed for both servos, 2:1 for the elevator and 1.5:1 for the rudder. Altogether the C-Tail weighs 87 g.

The two control actions of this design are the horizontal tail deflection (elevator), and the vertical tail deflection (rudder). This class of tails is used in conventional fixed-wing aircraft,

with the notable exception that there are no fixed surfaces (stabilizer), thus reducing the need for additional structure and therefore its weight.

C. V-Tail

The V-Tail is composed of a 0.044 m^2 fixed surface, which provides longitudinal and lateral stability to the ornithopter and two forked ruddervators with 0.037 m^2 surfaces, which provide the longitudinal and lateral-directional control, as shown in Fig. 4.

Several ornithopter designs have opted for a V-Tail. The Robird Bald Eagle and peregrine Falcon [12], as well as the Dove [13], have adopted a traditional V-Tail configuration. The Festo SmartBird [14] has a low dihedral inverted V-Tail, supplemented by a vertical stabilizer.

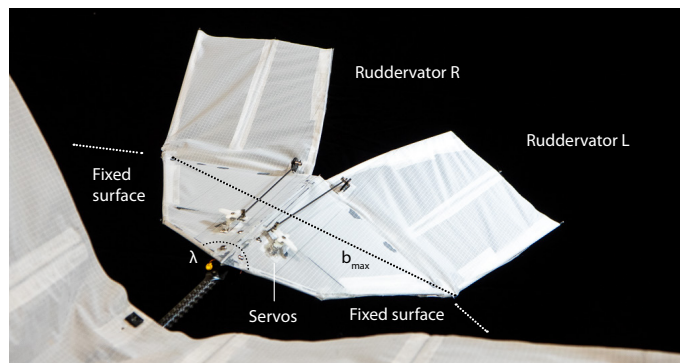


Figure 4. Photo of the inverse V-Tail configuration showing the stabilizing fixed surface as well as the two ruddervators.

The V-tail design has tail's spread, λ in Fig. 4, of 120 deg to reach the optimum moment-to-drag ratio (measurement of the ability of the tail to turn the bird) [15], [16]. The aspect ratio was trimmed to $b_{max}^2/S = 1.08$, while maintaining the total surface and chord to allow comparison between the three tails. Note that b_{max} is the maximum continuous span, see Fig. 4, considering that any section behind this line generates drag but not lift [15], [17], [18]. S is the total surface of the tail. The AR was set to this value so the tail is notably insensitive to the variation of the flow velocity and direction, what makes it the best solution to function in the steady and unsteady flow conditions of normal and slow flights [17]. An inverted V-Tail, i.e. with a negative dihedral angle, has been designed, to generate a yaw moment in the same direction than the roll moment, improving the lateral maneuverability.

The skeleton of the tail is composed of carbon fiber components. The forward section of the fixed surface consists of two CF plates of 0.6 mm thickness reinforced with 3 mm half-rods. This structure is connected to the fuselage tube through four compression adapters. Every CF profile is cut on a CNC router with a 3 mm end mill. Strong joints between plates and rods are achieved using a composite assembly method consisting of threaded Dyneema fibres with an epoxy matrix. The structure is covered with nylon ripstop fabric that is bonded to it with cyanoacrilate and ripstop tape, resulting in a 108 g Tail. The V-Tail has 2 DoF, i.e. the independent movement of each fin, provided by two servo motors housed

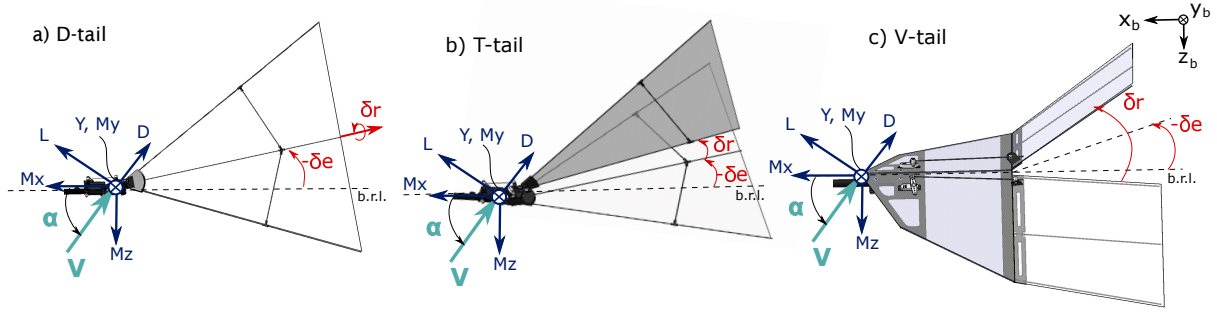


Figure 5. Surfaces deflections used in CFD analysis. Note that $\delta_1 = \alpha + \delta_e + \delta_r/2$, $\delta_2 = \alpha + \delta_e - \delta_r/2$ are the right and left ruddervator incidence angles. b.r.l. is the body reference line (x_b)

within holes in the CF plates. The ruddervators are linked to the servos via pushrods with a 1.2:1 reduction.

With this new tail design, we propose an alternative mechanism for controlling the roll angle without the need of introducing actuators on the main wing. As in the rest of the tails, the longitudinal and lateral-directional control variables are coupled. In this case, the control variables are defined as: $\delta_e = \frac{\delta_1 + \delta_2}{2}$ and $\delta_r = \frac{\delta_1 - \delta_2}{2}$. Where δ_1 and δ_2 corresponds to the right and left ruddervator deflection respectively, and δ_e and δ_r are the symmetrical and non-symmetrical deflection, called elevator and rudder deflections, defined in Fig. 5.

IV. TAIL AERODYNAMICS

In order to analyze the performance of the tails at different control deflections, an aerodynamic analysis has been carried out using Computational Fluid Dynamics (CFD) in a commercial software. The C-Tail is not featured in this analysis since longitudinal performance is similar to the D-Tail (which has been corroborated in the experiments) and no large lateral coupling is expected by design. Moreover, this tail configuration has been extensively studied in aircrafts. Thus, we focus on the more bio-inspired D and V tails which, in turn, has a strong coupling in lateral and longitudinal loads. Through the results obtained, an aerodynamic model of each tail is proposed and identified with a least-squares regression factor of about 97%. Additionally, a comparison of performances is provided.

A. CFD setup

A $k-\omega$ RANS model with Shear Stress transport is used in this simulation. This incompressible flow model is commonly used in both low and high Reynolds aerodynamics [19], with a pressure-velocity coupled scheme. The tails are modeled as 2 mm thickness flat surfaces (Fig. 6). Each configuration is meshed with ≈ 3 M tetrahedrons elements. Static simulations have been performed for $\alpha = [-30, 30]^\circ$ and $V = 4\text{m/s}$ (design velocity) in the entire range of control deflections of each tail $\delta_{e,r} = [-30, 30]^\circ$ (see Figure 5). The computation time is 2-3 days for each tail (32 cores CPU, 128 GB RAM). The data for negative deflections have been reconstructed assuming symmetry, giving 729 simulated configurations, altogether.

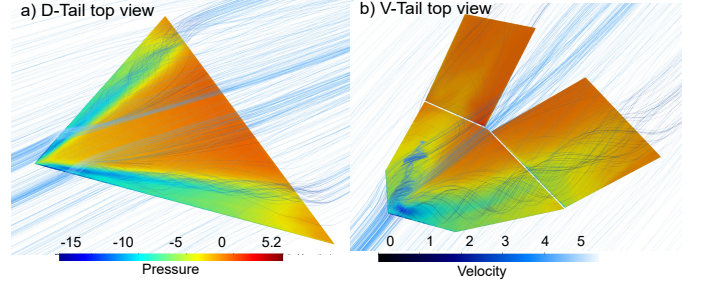


Figure 6. Pressure contours and streamlines over the tails at $\alpha = 20^\circ$, $\delta_e = -10^\circ$ and $\delta_r = 20^\circ$.

B. Modeling and results

The results for each tail (see Fig 5) have been post-processed to obtain the force and moments coefficient. Thus, denoting the forces as $F = [L, D, Y]$, and the moments as $M = [MX, MY, MZ]$, the coefficients are $c_F = F/0.5\rho V^2 S_t$ and $c_M = M/0.5\rho V^2 S_t c_t$, which are the lift, drag and lateral force, and roll, pitch and yaw moment tail's coefficients, respectively. Notice then, every force and moment is given in body axes, except c_L and c_D which are in aerodynamic reference frame, and measured at the leading edge of the tail.

1) *D-tail aerodynamics*: The proposed model reads

$$\begin{aligned} c_L &= c_{L,max} \sin(a_\alpha(\alpha + \delta_e)) \cos(\delta_r) \\ c_D &= c_{D,max} - (c_{D,max} - c_{D,0}) \cos(b_\alpha(\alpha + \delta_e)) \cos(\delta_r) \\ c_{MY} &= c_{MY,max} \sin(c_\alpha(\alpha + \delta_e)) \cos(\delta_r) \\ c_Y &= c_{Y,max} \sin(d_\alpha(\alpha + \delta_e)) \sin(\delta_r) \\ c_{MX} &= c_{MX,max} \sin(e_\alpha(\alpha + \delta_e)) \sin(\delta_r) \\ c_{MZ} &= c_{MZ,max} \sin(f_\alpha(\alpha + \delta_e)) \sin(\delta_r) \end{aligned}$$

The sinusoidal functions are chosen according to existing stall and delta-wing models [17], and the coefficients of the model are assumed constant. The $\cos(\delta_r)$ term accounts for the projection of the tail surface. The model also incorporates the stall effect, which implies that a maximum lift is reached, visible in Fig. 7. The lift-angle of attack slope is given by $a_\alpha \approx \frac{c_{L\alpha}}{c_{L,max}} \Big|_{\alpha < \alpha_{stall}}$ for small angles. The coefficients b_α and c_α are related to the drag and yaw moment slope. The drag is assumed symmetric with a $c_{D,0}$ offset. The lateral aerodynamics model the projection of lift for c_Y and c_{MZ} by $\sin(\delta_r)$ factor, and a relevant fact is the dependency of the

α as shown in Fig. 7. Besides aerodynamic stall affects greatly, making the UAV uncontrollable near this stall condition. The identified coefficients are summarized in Table II.

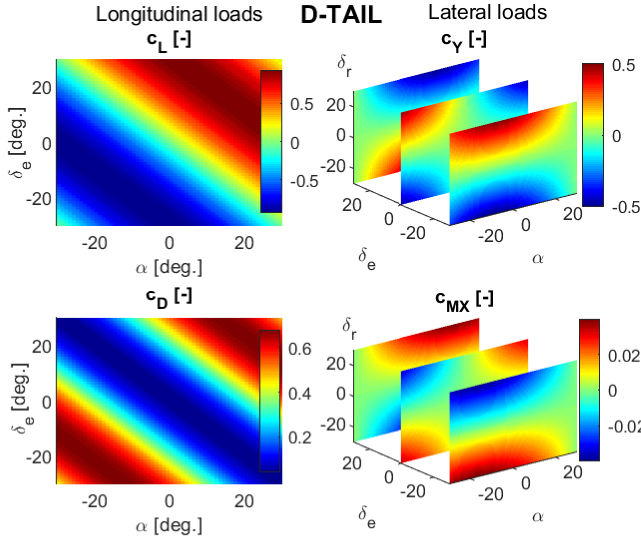


Figure 7. Relevant aerodynamic coefficients of the D-Tail c_L , c_D , c_Y and c_{MX} on tail's leading edge. Note that while all the longitudinal loads are multiplied by $\cos(\delta_r)$, only the $\delta_r = 0$ is shown since the influence of roll deflection only decreases the magnitude of the coefficients.

2) *V-Tail aerodynamics*: These aerodynamics differs substantially from the D-tail. The selected model intends to capture the stall of the wing and the flaps and the projection of the forces produced by each ruddervator.

$$\begin{aligned}
 c_L &= c_{L,max} \sin(a_\alpha \alpha + a_{\delta_e} \delta_e) \\
 c_D &= c_{D,max} - (c_{D,max} - c_{D,0}) \cos(b_\alpha \alpha + b_{\delta_e} \delta_e) \\
 c_{MY} &= c_{MY,max} \sin(c_\alpha \alpha + c_{\delta_e} \delta_e) \\
 c_Y &= c_{Y,max} \cos(d_\alpha (\alpha + \delta_e)) \sin(d_\alpha \delta_r / 2) \\
 c_{MX} &= c_{MX,max} \cos(e_\alpha (\alpha + \delta_e)) \sin(e_\alpha \delta_r / 2) \\
 c_{MZ} &= c_{MZ,max} \cos(f_\alpha (\alpha + \delta_e)) \sin(f_\alpha \delta_r / 2)
 \end{aligned}$$

The main difference in the longitudinal model is the different slopes for α and δ_e since they have different surfaces. Indeed, the effect of δ_r is negligible. The lateral performance is modeled taking into account the difference in lift of the ruddervators, and this is not affected by the sign of α .

The lateral moments on the overall bird can be composed by three effects: 1) The roll moment due to the difference in lift in both flaps, 2) The dihedral effect, which causes a yaw moment due to the difference in lift projected in the horizontal plane, and 3) The effect of the difference in drag in the flaps. The results show a good agreement with the design criteria and the expected forces, as it can be seen in Fig. 8.

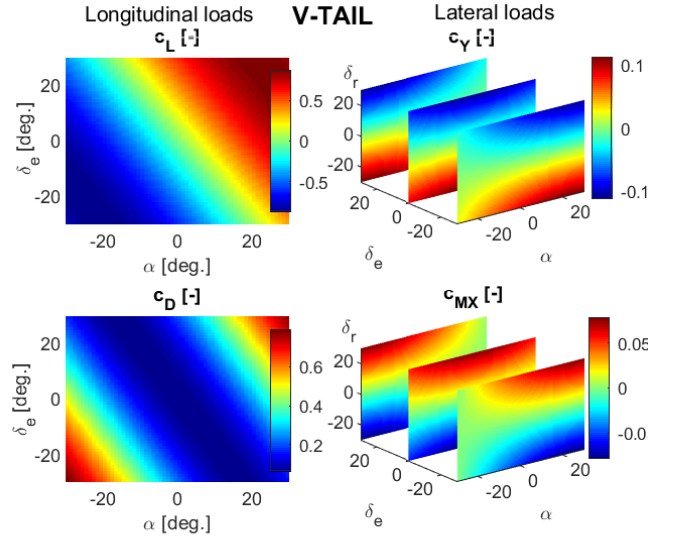


Figure 8. Relevant aerodynamic coefficients of the V-Tail c_L , c_D , c_Y and c_{MX} on tail's leading edge. Note that the moments created at the CG will differ.

Table II
IDENTIFIED PARAMETERS OF THE TAIL'S AERODYNAMIC MODELS

Parameter	D-TAIL	V-TAIL
$c_{L,max}$	0.94	0.88
a_α	2.92	2.32
a_{δ_e}	2.92	1.43
$c_{D,max}$	0.36	0.46
$c_{D,0}$	0.04	0.06
b_α	4.23	3.12
b_{δ_e}	4.23	1.72
$c_{MY,max}$	-0.65	-0.55
c_α	2.26	1.71
c_{δ_e}	2.26	1.23
$c_{Y,max}$	-1.02	-0.36
d_α	2.3	1.3
$c_{MX,max}$	0.08	0.22
e_α	1.9	1.48
$c_{MZ,max}$	0.64	0.33
f_α	1.94	1.2

3) *Aerodynamic performance comparison*: The CFD simulations show that regarding lift and hence pitch control capability, both tails have similar performance. The maximum lift coefficient of the V-Tail is slightly smaller, which may be due to the separation of the flaps (see Table II). However, stall occurs earlier on a D-tail than on a V-Tail. For a null deflection, stall occurs at $\alpha_{stall}|_{\delta_e=0} = 31$ and 38° for the D and V-Tail respectively, point at which the control capability starts decreasing. At flight condition $\alpha = 20^\circ$, stall occurs at elevator deflections of $\delta_{e,stall}|_{\alpha=20^\circ} = 11$ and 30° . This implies that while the longitudinal control capability is slightly higher in the D-tail, the operating range is wider in the V-Tail, as shown in first subplot in Fig. 9. For a better comparison we define the following indexes 'highlighting' the difference of moment coefficients at the CG as

$$\begin{aligned}
 I_{MY} &= -\text{sign}(\delta_e)(c'_{MY,V-T} - c'_{MY,D-T}), \\
 I_{MX} &= \text{sign}(\delta_r)(c'_{MX,V-T} - c'_{MX,D-T}), \\
 I_{MZ} &= \text{sign}(\delta_r)(c'_{MZ,V-T} - c'_{MZ,D-T}),
 \end{aligned}$$

where the c' are coefficients translated to the CG, and subscripts $D-T$ and $V-T$ are referred to the corresponding tail. From Fig. Fig. 9 we observe that the lateral control capacity varies significantly between the D and V-Tail (yaw moment c_{MZ} and lateral force c_Y). While the V-Tail performs better

at low angle of attack (independently of whether it is negative or positive) the lateral maneuverability is higher in the D-tail in a small range of high positive angle of attack. Finally, the roll control capability depends on α for the D-tail, which is not the case for the V-Tail. Fig. 7 and 8 show that the roll moment is negligible in the D-tail, except for very high deflections. As a reference, at a typical trim condition $\alpha = 20^\circ$, $\delta_e = -10^\circ$, the c_{MX} produced by the V-Tail is about 6 times greater than D-Tail. The relevance of the capability to produce roll, resides in

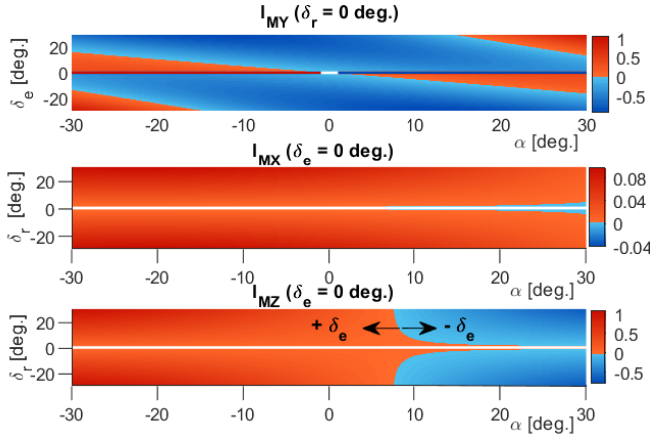


Figure 9. Comparative index between V and C-Tail for pitch, roll and yaw moment. Red zone means better performance for V-tail than D-tail, the opposite occurs in blue zones. The boundary between these zones for I_{MX} and I_{MY} shifts to left or right if δ_e increases or decreases respectively.

that the z and x inertia moments ratio $I_{zz}/I_{xx} \approx 4$ and hence the kinematics in roll will be faster than in yaw. On the other hand, the efficiency of the V-Tail is higher if we compare the control authority in terms of the deflected surface, since half the surface of the V-Tail is fixed. Certainly, Fig. 9 (mid) shows that the V-tail performs better in roll regardless of position. Lastly, the yaw control authority (Fig. 9 bottom) of the D-Tail and the V-Tail depends mainly of the angle of attack. This boundary decreases with δ_e , highlighting the importance of the trim elevator deflection, which affects the lateral dynamics of the ornithopter.

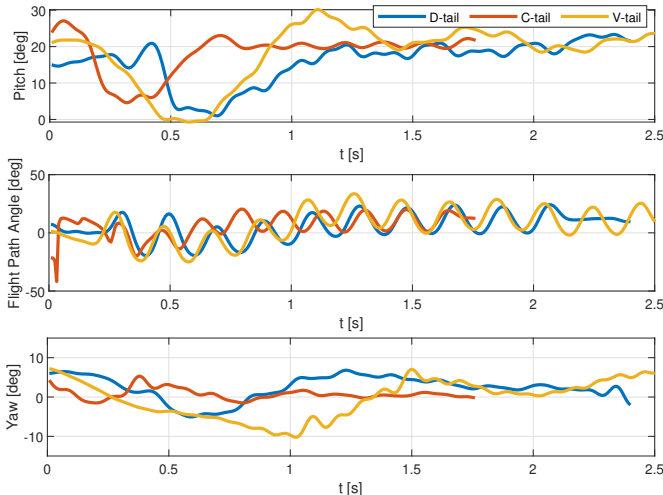


Figure 10. Response during controlled flight tests for the different tails. $\theta_{ref} = 20$ deg. Top: Pitch response. Center: Flight path angle response. Bottom: Yaw response during longitudinal flight.

V. FLIGHT EXPERIMENTS

In this section we describe the experimental characterization of the flight dynamics of the ornithopter, to evaluate the different performances of the tails. This is done for both longitudinal and lateral-directional dynamics. All the tests are performed using an Optitrack Motion Capture System and a custom autopilot similar to the one presented in [20] and [6]. The Optitrack consists on 28 infrared cameras which provide measurements of the attitude by roll, pitch and yaw Euler angles (ϕ, θ, ψ), and position of the CG in the earth reference frame (x_E, y_E, z_E). The measurements are sent to the onboard autopilot via VRPN protocol, which computes the control actions at 120 Hz. The flight path angle γ and the heading χ are calculated from this data. A PI controller is implemented and tuned experimentally to achieve the ‘best’ performance for each tail configuration. Measurement noise is reduced by an IIR low-pass filter with a cutoff frequency of 10 Hz, hence the flapping-induced oscillations at 3.5–5 Hz are visible in the experimental data.

A. Longitudinal Flight Tests

For these tests we implement a pitch control and an additional lateral yaw control to force the longitudinal flight condition. Thus, Fig. 10 shows the responses of a pitch controlled ascending flight test for each tail with pitch reference $\theta_{ref} = 20$ deg, in three plots: pitch, flight path angle and yaw. Notice that, the pitch angle converges to $\theta = 20$ deg for the three tails, indicating a stable longitudinal flight. However, the best performing tail in terms of faster convergence is the C tail, because the vertical rudder maintains the conditions closer to the longitudinal, as it can be seen in the yaw. In theory, D and C tails should perform similarly because of their equal horizontal surface, but D-tail’s strong coupling between the longitudinal and lateral-directional dynamics downgrades its performance. Although it is not shown, these results are consistent across all the tests and for different values of $\theta_{ref} \in [0, 30]$ deg.

Finally, it is worth mentioning that the value of the flight path angle after an initial transient remains around 12.8 deg for all the tails. This suggests a proportional relationship between the flight path and the pitch angles, thus allowing the control of the flight-path angle indirectly through the pitch.

B. 3D Lateral-directional Tests

To evaluate the lateral-directional maneuverability contribution of each tail, we conducted several tests consisting on aggressive heading maneuvers to obtain an estimate of the maximum turning rate. All the turning maneuvers are three dimensional due to the coupling between the longitudinal and lateral dynamics, albeit the previous controller is used to stabilize the longitudinal dynamics. The results across three different tests are collected in Fig. 11, where it is shown the averaged values and a max/min band for the turning rate, heading, lateral control input and the (x, y) trajectory in the horizontal plane.

The benchmark maneuver consists of throwing manually the robot from point $(x, y) = (0, 0)$ with a fixed 75-80% flapping

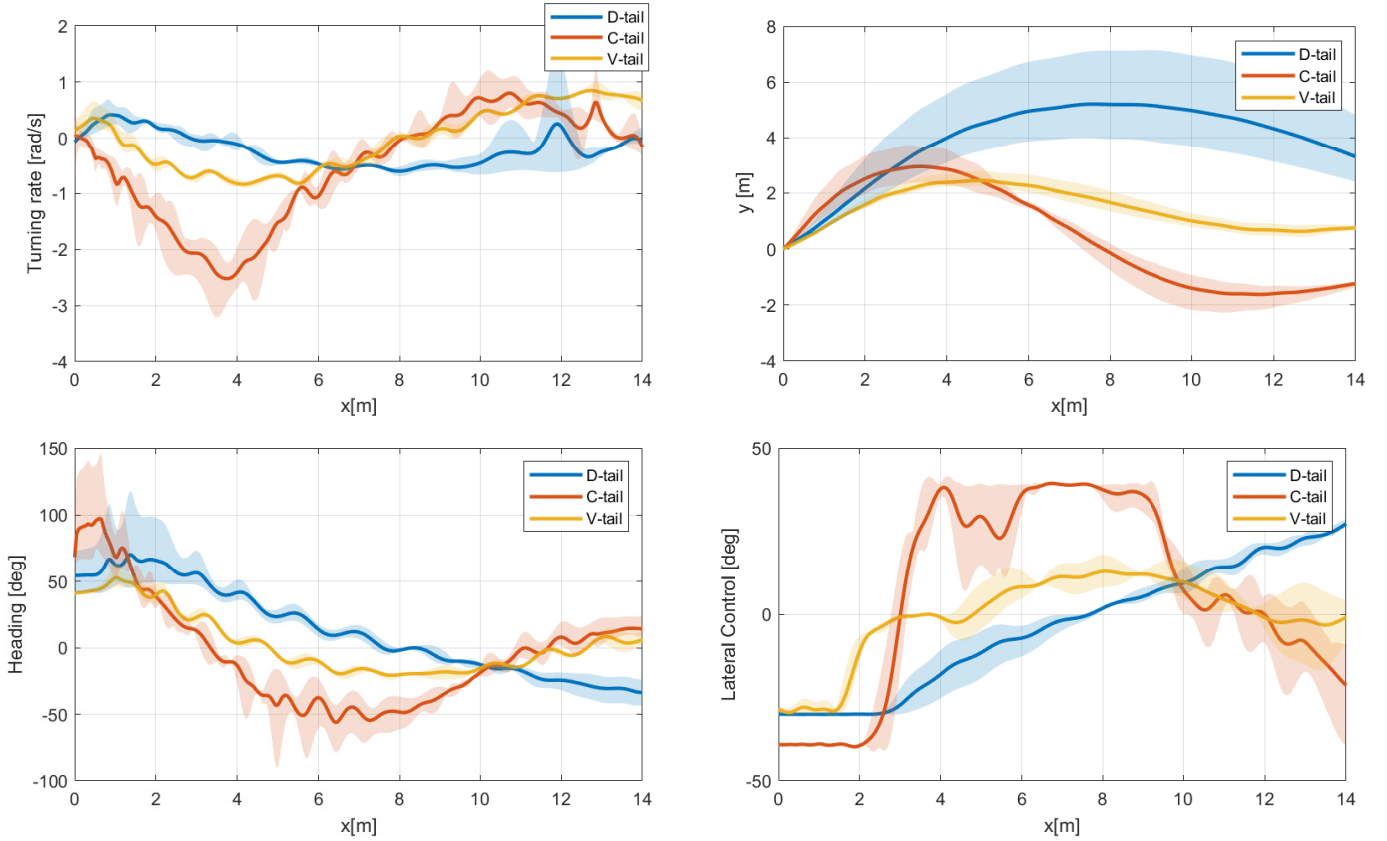


Figure 11. Averaged turning rate, heading, trajectory, and lateral control signal for three 3D lateral-directional tests. The mean values of the tests (lines) are plotted with the maximum and minimum bands, in function of x_E position.

throttle, and the flight controller regulates the pitch to maintain the level flight and imposes zero heading (parallel to $y = 0$) thereafter. The results are consistent between tests.

The turning rate ω is approximated as the one of a steady level banked turn and calculated as $\omega = V/R$ with $R = V^2/g\sqrt{n^2 - 1}$ and $n = 1/\cos\phi$, where V is the velocity and R the turning radius. Note that the assumptions of a steady level banked turn do not hold during the whole flight. However, this calculation remains as an useful approximation to conduct a comparative study between the tails. Thus, the C-tail shows the maximum magnitude of the turning rate during the first turn of the maneuver and the D-tail and V-tail share similar magnitudes (see Fig. 11).

Comparing the heading angle, the D-tail does not reach the desired 0 deg reference, while the V-tail and C-tail converge to a region around it. This proves that the D-tail performs worse in lateral turns as can be also observed in the (x, y) trajectory. The trajectory with the D-tail shows a large deviation from the initial position when compared to its counterparts. As a consequence, the D-tail should not be considered as a viable option above V and C-tails for fast turning three dimensional maneuvers.

Let compare the V and C-tail. The maximum turning-rate magnitude for the C-tail is 3.2 rad/s, and 0.9 rad/s for the V-tail. This corresponds with the C-tail having a minimum heading angle of -90 deg while the V-tail shows a minimum of -25 deg. The maximum of y is 2.8 m and 3.8 m for the

V-tail and C-tail, respectively. This shows that the peak value of the heading and y are greater in the C-tail. Looking at the control action, maximum control effort is needed most of the time during the C-tail flights, while for the V-tail is only needed briefly during the initial flight instants. This has the drawback of limiting the flight envelope of the C-tail.

To sum up, the experimental tests show: 1) the D-tail is not a good choice for three dimensional maneuvers; 2) C and V-tails can perform fast lateral maneuvers, but the peak values are consistently greater in the C-tail; 3) the V-tail shows less control effort than the C-tail. Thus, from this analysis of the flight tests we can conclude that the V-tail is more efficient control-wise, contributes positively to the three dimensional maneuverability and hence, it should be preferred over the other concepts for flapping-wing robots with only tail control surfaces.

To prove the full capabilities for lateral-directional flight of the V-tail, we performed an autonomous stable level turn. The lateral control variable is set to a constant maximum value, and the flight path angle is controlled as explained in Section V-A. The results are shown in Fig. 12. The turning radius and the mean turning-rate magnitude are 3.7 m and 1.6 rad/s, respectively. Note that the magnitude of the mean turning rate is far greater than the maximum turning-rate magnitude obtained from the tests in Fig. 11. This implies that the previous test does not show the full performance of the V-tail, and is greater than expected.

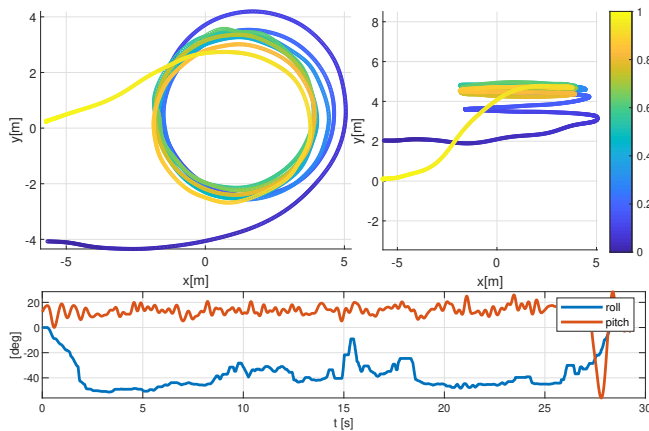


Figure 12. Stable three dimensional autonomous flight using the V tail. Top: 3D trajectory. The colorbar represents the normalized time. Bottom: Roll and pitch angles during flight.

The same maneuver was attempted with the C-tail but we could not achieve a stable level turn, and the C-tail showed to be unstable when conducting lateral turns for prolonged periods of time. The high deviation shown by the C-tail in the previous tests could be a symptom of this unstable behavior. We conjecture that the C-tail is unstable for prolonged aggressive lateral maneuvers in the same direction.

VI. CONCLUSIONS

The lightweight requirement in bird-scale flapping-wing limits the availability of control surfaces and lowers their maneuverability. Therefore, a well-designed actuated tail plays an important role in the control of an ornithopter and its flight stability. In this paper we present three tail designs, their aerodynamic model based on CFD and their in-flight performance.

The aerodynamic analysis highlights that the moments of the D-Tail depend on the sign of the angle of attack. This has a substantial impact on the control of flapping-wing robots as there are large variations due to the flapping perturbation. In the longitudinal direction, the undesired effect of stall occurs earlier in a D-Tail and C-Tail, leading to a narrower operating range and lower lateral performance than that of a V-Tail. Additionally, the V-Tail is capable of generating a substantial roll torque, a desirable characteristic for maneuverability.

Experimental characterization of the longitudinal and lateral direction maneuverability is provided for the three tails. Longitudinally, the results show that all the tails perform similarly, with minor differences in the settling time. However, the D-tail shows stronger coupling with the lateral-directional dynamics as the 3D tests show that the D-tail is not able to perform lateral turns consistently. On the contrary, the C and V-tails are able to perform aggressive heading maneuvers. Moreover, when testing for steady banked level turns, the V-tail is the only one showing stable performance, with a turning radius of 3.7 m at a turning rate of 1.6 rad/s. Overall the V-tail performs better in most maneuvers.

REFERENCES

- [1] M. H. Sadraey, *Aircraft design: A systems engineering approach*. John Wiley & Sons, 2012.
- [2] E. Ajanic, M. Feroskhan, S. Mintchev, F. Noca, and D. Floreano, "Bioinspired wing and tail morphing extends drone flight capabilities," *Sci. Robot.*, vol. 5, p. eabc2897, 2020.
- [3] J. Gerdes, A. Holness, A. Perez-Rosado, L. Roberts, A. Greisinger, E. Barnett, J. Kempny, D. Lingam, C.-H. Yeh, H. A. Bruck *et al.*, "Robo raven: a flapping-wing air vehicle with highly compliant and independently controlled wings," *Soft Robotics*, vol. 1, no. 4, pp. 275–288, 2014.
- [4] Z. J. Jackowski, "Design and construction of an autonomous ornithopter." Ph.D. dissertation, Massachusetts Institute of Technology, 2009.
- [5] M. S. Deshmukh and A. M. Dharme, "Design and construction of an ornithopter."
- [6] R. Zufferey, J. Tormo-Barbero, M. M. Guzman, F. Javier Maldonado, E. Sanchez-Laulhe, P. Grau, M. Perez, J. A. Acosta, and A. Ollero, "Design of the high-payload flapping wing robot e-flap," *IEEE Robotics & Automation Letters*, 2021.
- [7] R. Lopez-Lopez, V. Perez-Sanchez, P. Ramon-Soria, A. Martín-Alcántara, R. Fernandez-Feria, B. Arrue, and A. Ollero, "A linearized model for an ornithopter in gliding flight: Experiments and simulations," in *2020 IEEE International Conference on Robotics and Automation (ICRA)*. IEEE, 2020, pp. 7008–7014.
- [8] M. Hassanalian, A. Abdelkefi, M. Wei, and S. Ziaei-Rad, "A novel methodology for wing sizing of bio-inspired flapping wing micro air vehicles: theory and prototype," *Acta Mechanica*, vol. 228, no. 3, pp. 1097–1113, 2017.
- [9] A. Perez-Rosado, H. A. Bruck, and S. K. Gupta, "Enhancing the design of solar-powered flapping wing air vehicles using multifunctional structural components," in *ASME 2015 International Design Engineering Technical Conferences and Computers and Information in Engineering Conference*. American Society of Mechanical Engineers Digital Collection, 2015.
- [10] X. Zhou, X. Jin, Y. XU, and L. Zhang, "The Research and Design of Experimental Prototype in Flapping-Wing Micro-Air- Vehicles," *Advances in Natural Science*, vol. 7, no. 3, pp. 1–7, 2014.
- [11] J. H. Park and K.-J. Yoon, "Designing a biomimetic ornithopter capable of sustained and controlled flight," *Journal of Bionic Engineering*, vol. 5, no. 1, pp. 39–47, 2008.
- [12] G. A. Folkertsma, W. Straatman, N. Nijenhuis, C. H. Venner, and S. Stramigioli, "Robird: a robotic bird of prey," *IEEE robotics & automation magazine*, vol. 24, no. 3, pp. 22–29, 2017.
- [13] W. Yang, L. Wang, and B. Song, "Dove: A biomimetic flapping-wing micro air vehicle," *International Journal of Micro Air Vehicles*, vol. 10, no. 1, pp. 70–84, 2018.
- [14] Festo. Smartbird-bird flight deciphered. [Online]. Available: <https://www.festo.com/group/en/cms/10238.htm>
- [15] A. L. Thomas, "On the tails of birds," *Bioscience*, pp. 215–225, 1997.
- [16] A. L. Thomas and A. Balmford, "How natural selection shapes birds' tails," *The American Naturalist*, vol. 146, no. 6, pp. 848–868, 1995.
- [17] A. L. Thomas, "On the aerodynamics of birds' tails," *Philosophical Transactions of the Royal Society of London. Series B: Biological Sciences*, vol. 340, no. 1294, pp. 361–380, 1993.
- [18] S. Fitzpatrick, "Tail length in birds in relation to tail shape, general flight ecology and sexual selection," *Journal of Evolutionary Biology*, vol. 12, no. 1, pp. 49–60, 1999.
- [19] S. Bogos, A. Dumitrache, and F. Frunzulica, "Turbulence models in cfd simulation of low-reynolds number airfoils flow," vol. 1648, 03 2015, p. 500006.
- [20] F. J. Maldonado, J. A. Acosta, J. Tormo-Barbero, P. Grau, M. M. Guzmán, and A. Ollero, "Adaptive nonlinear control for perching of a bioinspired ornithopter," in *Proceedings of the 2020 IEEE/RSJ International Conference on Intelligent Robots and Systems (IROS)*, 2020.